PHYSICAL REVIEW B **101**, 205104 (2020)

Topological semimetal in an sp^2-sp^3 hybridized carbon network with nodal rings

Kun Bu,[1,2] Jian-Tao Wang,[1,2,3,*] Hongming Weng,[1,2,3] and Changfeng Chen[4]

[1]*Beijing National Laboratory for Condensed Matter Physics, Institute of Physics, Chinese Academy of Sciences, Beijing 100190, China*
[2]*School of Physics, University of Chinese Academy of Sciences, Beijing 100049, China*
[3]*Songshan Lake Materials Laboratory, Dongguan, Guangdong 523808, China*
[4]*Department of Physics and Astronomy, University of Nevada, Las Vegas, Nevada 89154, USA*

(Received 15 January 2020; accepted 14 April 2020; published 4 May 2020)

There have been several proposals that three-dimensional allotropes of carbon formed by graphene networks can support two types of topological nodal line semimetals: type A has closed nodal rings inside the first Brillouin zone (BZ), and type B has nodal lines traversing the whole BZ to be periodically connected. Among these proposals, it has been found that nearly all-sp^2 hybridized allotropes tend to hold A-type closed nodal rings, while the sp^2-sp^3 hybridized allotropes tend to hold B-type periodic nodal lines. Here we identify by *ab initio* calculations an sp^2-sp^3 hybridized carbon allotrope in $Pcca$ (D_{2h}^8) symmetry as a topological nodal line semimetal with two A-type closed nodal rings on the $k_y = 0$ and $k_y = \pi$ mirror planes, respectively. The projections of these two nodal rings onto (010) surfaces form concentric ellipses with different size. The drumhead surface states appear in the region enclosed by the bigger ring but disappear inside of the smaller ring. This is consistent with the distribution of the Berry phase calculated along the [010] periodic reciprocal lattice. An effective $k \cdot p$ model has been proposed, and the parameters have been obtained through fitting the *ab initio* results. The model can reproduce the nodal rings in the shape of an ellipse, satisfying the twofold rotational symmetry. Meanwhile, the simulated x-ray diffraction spectrum matches well with the recently reported distinct diffraction peaks found in the diamond-rich coatings on stainless steel substrate. These results establish a carbon phase with intriguing structural and electronic properties and expand our understandings about topological nodal lines in carbon networks.

DOI: 10.1103/PhysRevB.101.205104

I. INTRODUCTION

Topological semimetals have attracted great interest for their interesting physics and promising device applications [1,2]. Topological semimetals can be classified into Dirac [3,4] and Weyl [5,6] semimetals with isolated Dirac and Weyl nodes, or nodal line semimetals [7–22] with continuous line of nodes in the first Brillouin zone (BZ). A class of three-dimensional (3D) carbon allotropes has been reported holding topological nodal lines [22–35]. Generally, there are two types of nodal lines in the first BZ [23]: type A has a closed nodal ring inside the first BZ, and type B has nodal lines extending the first BZ. Among these proposals, usually all sp^2 hybridized carbon allotropes tend to hold A-type nodal rings such as Mackay-Terrones carbon crystal (MTC) [22], body-centered orthorhombic C_{16} (bco-C_{16}) [25], body-centered tetragonal C_{16} (bct-C_{16}) [26], and base-centered orthorhombic ors-C_{16} [30]; while sp^2-sp^3 hybridized carbon allotropes tend to hold B-type nodal lines such as interpenetrated graphene network C_6 (ign-C_6) [27], simple orthorhombic C_{12} (so-C_{12}) [28], and orthorhombic C_{24} (oC24) [29]. These facts indicate that the configuration of nodal lines in 3D carbon network structures might be determined by the bonding types. However, very recently a new hexagonal series of topological nodal line carbon phases was proposed for all-sp^2 hybridized networks but holding B-type paired nodal lines on the edge of the first BZ rather than A-type closed nodal rings [34], which is well explained based on topological quantum chemistry theory [36] or symmetry-based indicator theory [37–39]. This finding suggests that bonding types do not play an essential role in determining the type of nodal lines, and the A-type closed nodal rings may also exist in sp^2-sp^3 hybridized carbon structures.

In this paper, to answer the question we report by *ab initio* calculations an sp^2-sp^3 hybridized carbon phase in $Pcca$ (D_{2h}^8) symmetry that has a 16-atom orthorhombic primitive-unit cell, thus called oP16 carbon. This carbon allotrope is identified through a systematic structure search process as well as R16 carbon [40] and is energetically more stable than the previously predicted and synthesized R16 [40] and BC8 [41–44] carbon phases. Its dynamical stability has been confirmed with phonon spectrum calculations. The simulated x-ray diffraction pattern matches well with the recently reported distinct diffraction peaks found in the diamond-rich coatings on stainless steel substrate [45], suggesting a viable experimental synthesis route. Electronic band structures show that oP16 carbon is a candidate of a topological nodal line semimetal protected by inversion (P) and time-reversal (T) symmetry. Unlike the previously reported sp^2-sp^3 hybridized carbon allotropes [27–29], oP16 carbon holds two A-type closed nodal rings on the $k_y = 0$ and $k_y = \pi$ mirror planes. Moreover, when the two nodal rings are projected onto the (010) surface, a nearly flat topologically nontrivial surface

---

[*] wjt@aphy.iphy.ac.cn

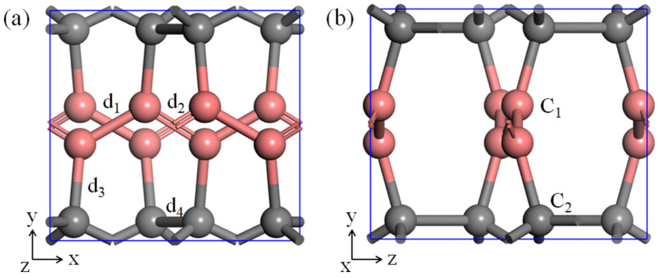

FIG. 1. The top (a) and side (b) view of oP16 carbon. It has a 16-atom orthorhombic primitive-unit cell in *Pcca* (D_{2h}^8) symmetry with the lattice parameters $a = 4.6464$ Å, b=4.2766 Å, and $c = 5.1325$ Å, occupying the two 8f Wyckoff positions of (0.3799, 0.5812, 0.5311) and (0.0936, 0.9189, 0.1087), denoted by C_1 (red) and C_2 (black), while C_1 atoms are in sp^2 sites and C_2 atoms are in sp^3 sites.

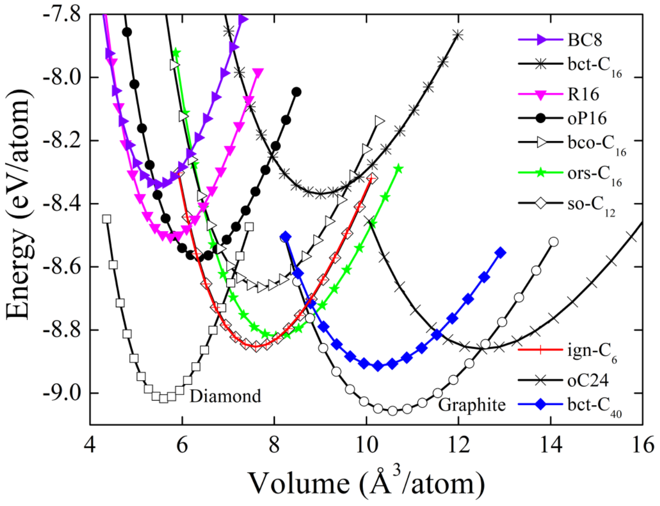

FIG. 2. The calculated total energy as a function of volume per atom for diamond, graphite, BC8, bct-C_{16}, R16, oP16, bco-C_{16}, ors-C_{16}, so-C_{12}, ign-C_6, oC24, and bct-C_{40} carbon.

state can be found between two projected Γ-centered concentric nodal rings. This distinct topological nodal line semimetal can be systematically understood from the low anisotropy of its first BZ and the symmetry-based indicator theory [37–39].

II. COMPUTATIONAL METHODS

Our *ab initio* calculations are carried out using density functional theory (DFT) as implemented in the Vienna *ab initio* simulation package (VASP) [46]. The generalized gradient approximation (GGA) developed by Armiento-Mattsson (AM05) [47] is adopted for the exchange-correlation potential. The all-electron projector augmented wave (PAW) method [48] is used which treats the $2s^22p^2$ electrons as valence electrons. A plane-wave basis set with an energy cutoff of 800 eV is adopted. Forces on the ions are calculated using the Hellmann-Feynman theorem with a full geometry optimization. The convergence criteria for electron self-consistent relaxation is 10^{-8} eV and the ionic relaxation is 0.001 eV/Å. The electronic band structures are calculated using a hybrid density functional based on the Heyd-Scuseria-Ernzerhof scheme (HSE06) [49]. To further explore the topological electronic properties of oP16 carbon, we establish a tight-binding (TB) model using maximally localized Wannier functions (MLWFs) [50,51] for carbon p_z orbitals and calculate the Berry phase with the WANNIER TOOLS package [52]. Phonon band structures are calculated with PHONOPY package [53].

III. RESULTS AND DISCUSSION

We first characterize the structural properties of oP16 carbon. It has an orthorhombic primitive-unit cell with 16 atoms in *Pcca* (D_{2h}^8, No. 54) symmetry. The equilibrium lattice parameters are estimated to be $a = 4.6464$ Å, $b = 4.2766$ Å, and $c = 5.1325$ Å, with carbon atoms occupying two nonequivalent 8f Wyckoff positions of (0.3799, 0.5812, 0.5311) and (0.0936, 0.9189, 0.1087), denoted by C_1 and C_2, respectively, as shown in Fig. 1. The carbon atoms at C_1 sites are all sp^2 hybridized, and the carbon atoms at C_2 sites are all sp^3 hybridized, showing a sp^2-sp^3 hybridized carbon network. There are four distinct bond lengths: two shorter bond lengths of 1.392 Å (d_1) and 1.353 Å (d_2) associated with $C_1(sp^2) - C_1(sp^2)$ and $C_1(sp^2) = C_1(sp^2)$; and two longer bond lengths of 1.503 Å (d_3) and 1.691 Å (d_4) associated with $C_1(sp^2) - C_2(sp^3)$ and $C_2(sp^3) - C_2(sp^3)$. There are also four distinct bond angles: $\angle C_1 = C_1\text{-}C_1 = 117.32^\circ$, $\angle C_1\text{-}C_1\text{-}C_2 = 123.39^\circ$, $\angle C_1 = C_1\text{-}C_2 = 119.22^\circ$, and $\angle C_1\text{-}C_2\text{-}C_2 = 105.63^\circ$.

Figure 2 shows the calculated energy vs volume per atom of oP16 carbon compared with diamond, graphite, and previously reported BC8 [41–44], bct-C_{16} [26], R16 [40], bco-C_{16} [25], ors-C_{16} [30], so-C_{12} [28], ign-C_6 [27], oC24 [29], and bct-C_{40} carbon [35]. The energetic data obeys the following stability sequence: bct-C_{40} > oC24 > ign-C_6 > so-C_{12} > ors-C_{16} > bco-C_{16} > oP16 > R16 > bct-C_{16} > BC8. We can see that oP16 carbon is a metastable phase less stable than diamond and graphite, but more stable than the previously reported BC8, bct-C_{16}, and R16 carbon. The equilibrium volume of oP16 carbon is 6.37 Å^3/atom, which is larger than those of R16 and BC8 carbon phases that are all comprised of 16 carbon atoms. By a Murnaghan fitting [54] of the energy-volume curves, we obtain the bulk modulus (B_0) of oP16 carbon as 370 GPa, which is smaller than 451 GPa for diamond, 407 GPa for BC8, and 386 GPa for R16 carbon, but larger than 250 GPa for bct-C_{16}, 315 GPa for bco-C_{16}, 298 GPa for ors-C_{16}, 322 GPa for so-C_{12}, 192 GPa for oC24, and 239 GPa for bct-C_{40} carbon. The calculated equilibrium structural parameters, total energy, and bulk modulus are listed in Table I.

To examine the dynamical stability of oP16 carbon, we have calculated the phonon band structures and partial density of states (PDOS), as shown in Fig. 3. There are two major peaks at around 1419 and 1044 cm^{-1}. The peak at around 1419 cm^{-1} is related to C_1 carbon atoms in sp^2 bonding, similar to the finding in all-sp^2 hybridized bco-C_{16} [25], while the peak at around 1044 cm^{-1} is related to C_2 carbon atoms in sp^3 bonding, similar to the finding in diamond. Meanwhile, there is an obvious phonon gap between 1381 and 1468 cm^{-1} at the X point, attributing to the distinct shorter sp^2 and longer sp^3 bonds. No imaginary frequency occurs through the entire

TABLE I. Calculated equilibrium structural parameters (lattice parameter a, b, c and α, volume per atom V_0, bond lengths d_{C-C}), total energy per atom E_{tot}, electronic band gap E_g, and bulk modulus (B_0) for diamond, BC8, bct-C_{16}, R16, oP16, bco-C_{16}, ors-C_{16}, so-C_{12}, ign-C_6, oC24, and bct-C_{40} carbon at zero pressure, compared to available experimental data [44,55].

Structure	Space group	Method	a (Å)	b (Å)	c (Å)	α (°)	V_0 (Å^3)	d_{C-C} (Å)	E_{tot} (eV)	E_g (eV)	B_0 (GPa)
Diamond	$Fd\bar{3}m$	AM05	3.552				5.60	1.538	−9.018	5.36	451
		Exp [55]	3.567				5.67	1.544		5.47	446
BC8	$Ia\bar{3}$	AM05	4.443				5.48	1.617	−8.340	3.58	407
		Exp [44]	4.450								
bct-C_{16}	$I4_1/amd$	AM05 [26]	6.578		3.330		9.01	1.360, 1.477	−8.369	Semimetal	250
R16	$R\bar{3}c$	AM05	4.514			90.88	5.75	1.466-1.755	−8.505	4.45	386
oP16	$Pcca$	AM05	4.646	4.277	5.133		6.37	1.353-1.691	−8.570	Semimetal	370
bco-C_{16}	$Imma$	AM05 [25]	7.806	4.877	3.237		7.70	1.382-1.459	−8.671	Semimetal	315
ors-C_{16}	$Cccm$	AM05 [30]	3.318	8.372	4.915		8.02	1.421-1.438	−8.810	Semimetal	298
so-C_{12}	$Pbcm$	AM05 [28]	4.313	8.604	2.461		7.61	1.406-1.520	−8.851	Semimetal	322
ign-C_6	$Cmmm$	AM05 [27]	5.899	6.281	2.459		7.60	1.406-1.522	−8.852	Semimetal	323
oC24	$Cmmm$	AM05 [29]	13.632	8.867	2.468		12.43	1.336-1.523	−8.858	Semimetal	192
bct-C_{40}	$I4/mmm$	AM05 [35]	12.901		2.460		10.25	1.412-1.516	−8.912	Semimetal	239

BZ and PDOS, thus confirming the dynamical stability of oP16 carbon.

We next discuss the electronic properties of oP16 carbon. Figure 4(a) represents the band structure at equilibrium lattice parameters. The valence and conduction bands with opposite parities cross each other near the Fermi level (E_F) to form several nodal points along the high-symmetric directions of Z-Γ, Γ-Y, T-Γ, X-U, R-X, and X-S in the bulk BZ due to the band inversion mechanism [22,56,57]. In fact, these inverted band structures lead to two A-type closed nodal rings on the $k_y = 0$ and $k_y = \pi$ mirror planes protected by the P and T symmetries, as shown in Fig. 4(b). The parity products for the occupied states at the time-reversal invariant momenta (TRIM) points are listed in Table II.

The presence of the two nodal rings can be explained within the symmetry-based indicator theory [37–39]. For an inversion symmetric system without spin-orbit coupling (SOC), the symmetry indicators $\mathbb{Z}_{2,2,2,4} = (z_{2,1}, z_{2,2}, z_{2,3}, z_4)$ are defined to indicate a nontrivial topological classification:

$$z_{2,\varepsilon} \equiv \sum_{\substack{\mathbf{K}\,\in\,\mathrm{TRIM} \\ \text{at } \{k_\varepsilon = \pi,\, \varepsilon = 1,2,3\}}} \frac{n_-^{\mathbf{K}} - n_+^{\mathbf{K}}}{2} \bmod 2$$

$$z_4 \equiv \sum_{\mathbf{K}\in\mathrm{TRIM}} \frac{n_-^{\mathbf{K}} - n_+^{\mathbf{K}}}{2} \bmod 4, \qquad (1)$$

where $n_\pm^{\mathbf{K}}$ is the number of occupied states having even (odd) parity at the TRIM points. For oP16 carbon, the symmetry indicator is calculated to be $(z_{2,1}, z_{2,2}, z_{2,3}, z_4) = (0, 1, 0, 0)$. According to Ref. [39], when $z_4 = 0$, 2 and $z_{2,i} = 1$, there should be two nodal rings on the $k_i = 0$, $k_i = \pi$ planes, respectively, or both the $k_i = 0$, $k_i = \pi$ planes are crossed by nodal lines for 2 mod 4 times. In oP16 carbon, the SOC induced band gap is about 0.0001 eV. It can be easily checked that when SOC is considered, oP16 carbon becomes a three-dimensional weak topological insulator.

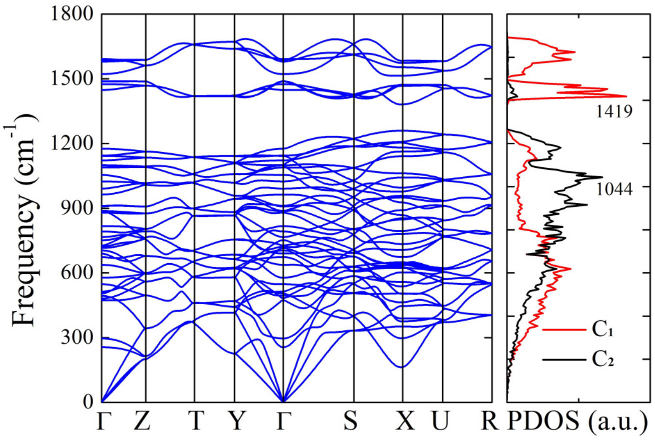

FIG. 3. Phonon band structures and density of states (PDOS) of oP16 carbon. The peak at around 1419 cm^{-1} is related to C_1 carbon atoms in sp^2 bonding, while the peak at around 1044 cm^{-1} is related to C_2 carbon atoms in sp^3 bonding.

Figure 4(c) shows the band decomposed charge density for the occupied state near the E_F of oP16 carbon, which indicates that the electron hopping happens mainly between the sp^2 hybridized C_1 atoms. Furthermore, as shown in Fig. 4(d) for the partial density of states (DOS), the energy bands near the E_F are mainly contributed by the p_z orbitals of C_1 atoms. To further explore the topological electronic properties of oP16 carbon, we have constructed an eight-band TB model based on the MLWFs constructed for the p_z orbitals of C_1 atoms by using the WANNIER90 package [50,51]. The calculated TB band structures are also plotted in Fig. 4(a) with red dashed lines. We can see that the TB band structures match well with

TABLE II. The parity products for the occupied states at the time-reversal invariant momenta (TRIM) points.

Γ (0.0,0.0,0.0)	Z (0.0, 0.0, 0.5)	T (0.5, 0.0, 0.5)	Y (0.5, 0.0, 0.0)
−	+	+	+
S (0.5, 0.5, 0.0)	X (0.0, 0.5, 0.0)	U (0.0, 0.0, 0.5)	R (0.5, 0.5, 0.5)
+	−	+	+

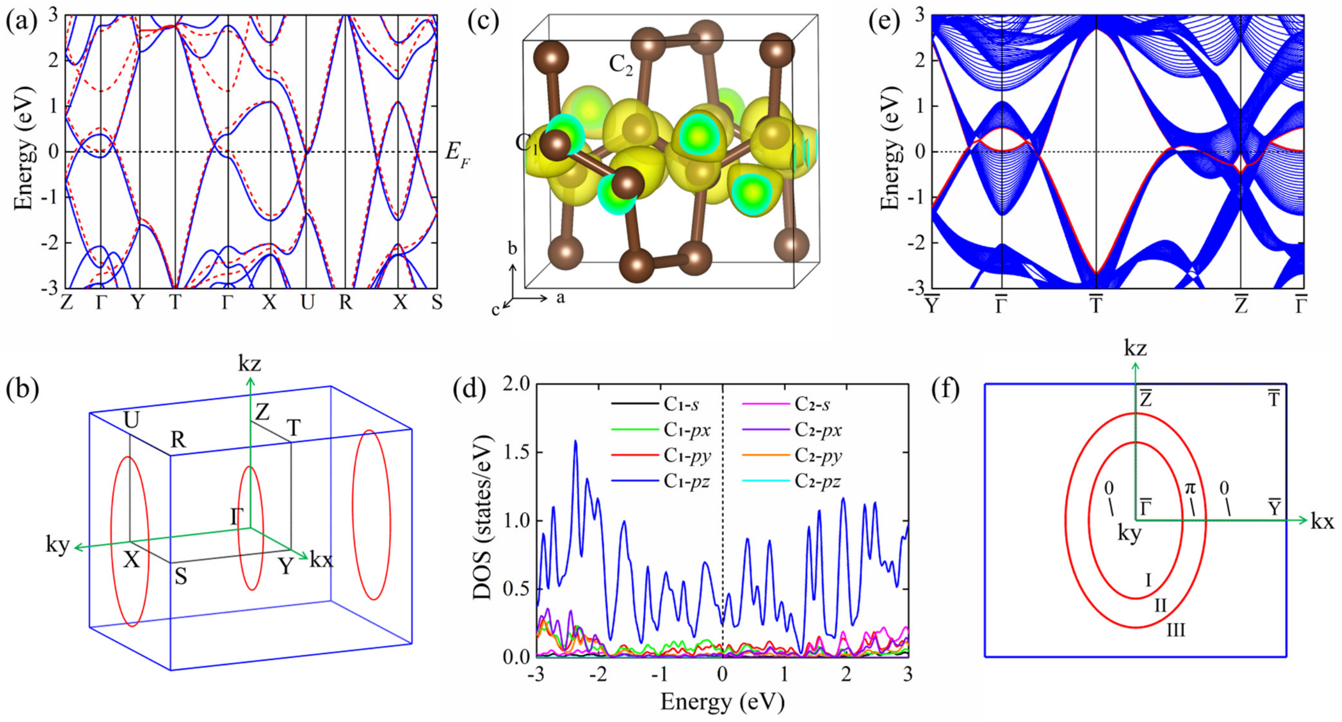

FIG. 4. (a) The calculated energy bands of oP16 carbon. The blue solid lines represent the band structures obtained from DFT methods, while the red dashed lines represent the band structures obtained from the TB model. (b) Two closed A-type nodal rings on the $k_y = 0$ and $k_y = \pi$ mirror planes in the 3D BZ of oP16 carbon. (c) The band-decomposed charge density isosurfaces (0.01 e/Å^3) for the occupied state around the E_F. (d) The partial density of states (DOS) for oP16 carbon. (e) The calculated (010) surface state obtained using 30-layer thick slab geometry along the [010] crystalline direction based on the TB model. (f) The projection of two nodal rings onto the (010) projected plane. The Berry phases inside the small nodal ring (zone I) and outside the large ring (zone III) are 0, while the Berry phase between the small and large nodal rings (zone II) is π.

the DFT band structures in the vicinity of E_F, indicating the validity of our TB model.

In order to investigate the surface state, we have built a 30-layer-thick slab geometry along the [010] crystalline direction terminated with C_1 atoms on both up and down surfaces, and the surfaces are not passivated by hydrogen atoms, based on the above TB model. Figure 4(e) shows the calculated (010) surface states. The projection of two nodal rings onto the (010) surface shows two concentric rings with different sizes [see Fig. 4(f)]. There is a topological nontrivial surface band between the projection of the large nodal ring and the small one. Along the $\overline{Y}-\overline{\Gamma}$ and $\overline{\Gamma}-\overline{T}$ directions, the surface state is visible [see Fig. 4(e)], while along the $\overline{Z}-\overline{\Gamma}$ directions, there is no surface state. This topologically nontrivial surface state should be detectable by angle-resolved photoemission spectroscopy (ARPES) experiments [58].

As a topological nodal line semimetal, the nontrivial surface states are to be protected by the topological invariant in bulk, i.e., the nontrivial Berry phase. To understand the surface states of oP16 carbon, we have calculated the Berry phase with the WANNIER TOOLS package [52]. We choose three lines [black solid lines in Fig. 4(f)] passing through the BZ along the k_y direction. The first one is inside of the small nodal ring (zone I); the second one is outside of the small ring but inside of the large one (zone II); and the third one is outside of the large nodal ring (zone III). The Berry phases, or Zak phases, accumulated along these periodic lines have been calculated to be 0, π, and 0 in regions I, II, and III, respectively. Thus the topological nontrivial surface state, known as the drumhead surface state [22], is expected to appear in the surface BZ where the Berry phase is of π.

Unlike the previously reported sp^2-sp^3 hybridized carbon allotropes, such as ign-C_6 [27], so-C_{12} [28], and oC_{24} [29], that have B-type paired nodal lines, this oP16 carbon has A-type closed nodal rings rather than the paired nodal lines of B type. To obtain a unified understanding of the type of topological nodal lines in 3D carbon network structures, we establish a two-band effective $k \cdot p$ model (see part (1) in the Supplemental Material [59]). It is shown that the nodal line can be described by an ellipse equation $m_1k_x^2 + m_3k_z^2 = -m_0$ on the $k_y = 0$ and $k_y = \pi$ mirror planes for oP16 and related carbon phases, while m_0 is related to the strength of the band inversion at the Γ point and $m_i (i = 1, 3)$ is related to the size and shape of nodal ring. The parameters m_0 and m_i can be obtained by fitting the *ab initio* results. The semimajor axis (X_1) and semiminor axis (X_2) of the ellipse are $\sqrt{-m_0/m_1}$ and $\sqrt{-m_0/m_3}$ (see Table S1 in Supplemental Material [59]), respectively. For oP16 carbon, $X_1 = 0.1636$ and $X_2 = 0.2984$ on the $k_y = 0$ plane; $X_1 = 0.2245$ and $X_2 = 0.3611$ on the $k_y = \pi$ plane. In the lattice model with scaled units, the boundary of the first BZ limits the value of k_x and k_z to be within [−0.5, 0.5]. If the lattice anisotropy is large enough, the ellipse of type-A nodal lines will change into periodically connected nodal lines of type B. For example, in ign-C_6, so-C_{12}, and oC_{24} carbon structures, $X_1 > 0.5$ and $X_2 < 0.5$, the ellipse extends outside of the first BZ along the k_x direction and leaves a pair of B-type nodal lines in the first BZ.

It is worth noting that the types of nodal lines in these carbon phases are essentially dependent on the *lattice anisotropy* of the first BZ rather than bonding type (see part (2) in Supplemental Material [59] for a detailed discussion of the anisotropic effect). To get a systematical understanding of the topological nodal lines found in carbon allotropes, here we define the lattice anisotropy coefficient $e = a_i/a_j$ (where a_i and a_j are the lattice parameters corresponding to the mirror plane that holds the nodal lines). We choose that $a_i \geqslant a_j$ so that $e \geqslant 1$. For cubic MTC and tetragonal bct-C_{16} carbon in all-sp^2 bonding, the e values are estimated to be 1.0, so that the nodal lines in MTC [22] and bct-C_{16} carbon [26] are nearly circles due to the lowest anisotropy coefficient; for orthorhombic ors-C_{16} and bco-C_{16} in an all-sp^2 hybridized network, the rotation symmetry has been lowered to a twofold rotation symmetry (C_2) with an anisotropy coefficient of 1.481 and 1.507, respectively, so the nodal lines in ors-C_{16} and bco-C_{16} are ellipses; for so-C_{12}, ign-C_6, and oC24 carbon in sp^2-sp^3 hybridized bonding, they have the same C_2 symmetry with a larger anisotropy coefficient of 1.753, 2.399, and 5.524, respectively, so that the nodal lines in so-C_{12}, ign-C_6, and oC24 carbon are B-type paired nodal lines. Moreover, although oP16 is in a sp^2-sp^3 hybridized network, its anisotropy coefficient e is estimated to be 1.105, which is even smaller than the all-sp^2 hybridized ors-C_{16} and bco-C_{16} carbon, showing a very low anisotropy. Thus, the nodal lines in oP16 carbon tend to form A-type closed *elliptic* rings rather than B-type nodal lines in pairs. As a result, the carbon allotropes with a low anisotropic lattice tend to form A-type nodal rings, while a high anisotropic lattice tends to form B-type nodal lines in the first BZ (see Table S2 in the Supplemental Material [59]).

We have further investigated the effect of strain on the electronic band structures for oP16 carbon. The calculated band structures with isotropic lattice strain of −5% and +5% for oP16 carbon are plotted in Fig. S3 in the Supplemental Material [59]. It is shown that the band inversion and nodal points in oP16 carbon can hold well under compression or tensile strain, showing the high robustness of the two nodal rings in oP16 carbon under possible structure deformation induced by applied strain.

Finally, to establish the experimental connection of oP16 carbon, we have simulated the x-ray diffraction (XRD) spectra, along with those of diamond, graphite, bct-C_{16} [26], bco-C_{16} [25], so-C_{12} [28], ign-C_6 [27], and R16 [40] carbon [see Fig. 5(a)] and compare with the experimental data from the diamond-rich coatings on stainless steel substrate [45], as shown in Fig. 5(b). Comparing with the reported bct-C_{16}, bco-C_{16}, so-C_{12}, ign-C_6, and R16 carbon phases, oP16 carbon shows a more complicated XRD pattern arising from the multiple bond lengths and bond angles. However, the simulated peaks (111) at 33°, (002) at 35°, (200) at 39°, and (020) around 42° match well with the measured XRD peaks [45]. This good match between the simulated and experimental XRD peaks strongly suggests oP16 as one of the experimentally discovered phases and indicates that oP16 can be derived from the diamond-rich coatings on stainless steel substrate [45].

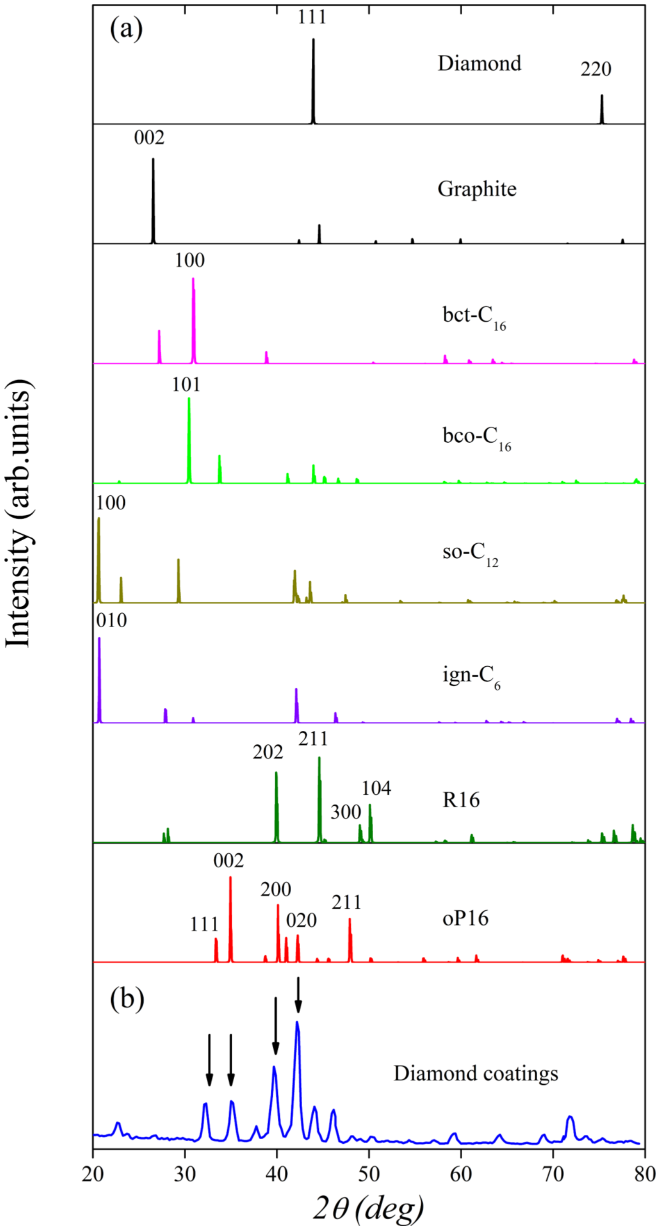

FIG. 5. (a) Simulated XRD patterns for diamond, graphite, bct-C_{16}, bco-C_{16}, so-C_{12}, ign-C_6, R16, and oP16 carbon phases. (b) Experimental XRD patterns for the diamond-rich coatings on stainless steel substrate [45]. The x-ray wavelength is 1.5406 Å with a copper source.

IV. CONCLUSION

In conclusion, we have proposed by *ab initio* calculations an sp^2-sp^3 hybridized carbon allotrope in *Pcca* (D_{2h}^8) symmetry that has a 16-atom orthorhombic primitive-unit cell, characterized as a topological nodal line semimetal with two A-type closed nodal rings on the $k_y = 0$ and $k_y = \pi$ mirror planes. The projections of these two nodal rings onto (010) surfaces form concentric ellipses, and a nearly flat topological nontrivial surface state is visible between the two projected rings. We find that such distinct topological nodal lines in carbon networks can be cohesively described within an ellipse model, and the type of nodal lines indeed depends on the lattice anisotropy rather than the bonding type. Meanwhile, the simulated x-ray diffraction pattern matches well with the recently reported distinct diffraction peaks found in the diamond-rich coatings on stainless steel substrate [45], suggesting a viable experimental synthesis route. These findings expand our understandings about topological nodal lines in carbon networks and pave the way for further studies in this very active research field.

ACKNOWLEDGMENTS

The authors thank Prof. Panagiotis Kotetes and Dr. Dexi Shao for very valuable discussions. This study was supported by the National Natural Science Foundation of China (Grants No. 11674364, No. 11974387, No. 11925408, and No. 11921004) and the Strategic Priority Research Program of the Chinese Academy of Sciences (Grants No. XDB33000000 and No. XXH13506-202). H.W. acknowledges support from the National Key Research and Development Program of China (Grants No. 2016YFA0300600 and No. 2018YFA0305700), the K. C. Wong Education Foundation (Grant No. GJTD-2018-01), the Beijing Natural Science Foundation (Grant No. Z180008), and the Beijing Municipal Science and Technology Commission (Grant No. Z181100004218001).

[1] H. Weng, X. Dai, and Z. Fang, J. Phys.: Condens. Matter **28**, 303001 (2016).
[2] N. P. Armitage, E. J. Mele, and A. Vishwanath, Rev. Mod. Phys. **90**, 015001 (2018).
[3] Z. Wang, Y. Sun, X. Q. Chen, C. Franchini, G. Xu, H. Weng, X. Dai, and Z. Fang, Phys. Rev. B **85**, 195320 (2012).
[4] Z. Wang, H. Weng, Q. Wu, X. Dai, and Z. Fang, Phys. Rev. B **88**, 125427 (2013).
[5] H. Weng, C. Fang, Z. Fang, B. A. Bernevig, and X. Dai, Phys. Rev. X **5**, 011029 (2015).
[6] X. Wan, A. M. Turner, A. Vishwanath, and S. Y. Savrasov, Phys. Rev. B **83**, 205101 (2011).
[7] A. A. Burkov, M. D. Hook, and L. Balents, Phys. Rev. B **84**, 235126 (2011).
[8] M. Phillips and V. Aji, Phys. Rev. B **90**, 115111 (2014).
[9] C. Fang, Y. Chen, H. Y. Kee, and L. Fu, Phys. Rev. B **92**, 081201(R) (2015).
[10] R. Yu, H. Weng, Z. Fang, X. Dai, and X. Hu, Phys. Rev. Lett. **115**, 036807 (2015).
[11] T. T. Heikklia and G. E. Volovik, New J. Phys. **17**, 093019 (2015).
[12] L. S. Xie, L. M. Schoop, E. M. Seibel, Q. D. Gibson, W. Xie, and R. J. Cava, APL Mater. **3**, 083602 (2015).
[13] K. Mullen, B. Uchoa, and D. T. Glatzhofer, Phys. Rev. Lett. **115**, 026403 (2015).
[14] Y.-H. Chan, C.-K. Chiu, M. Y. Chou, and A. P. Schnyder, Phys. Rev. B **93**, 205132 (2016).
[15] T. Bzdusek, Q. S. Wu, A. Ruegg, M. Sigrist, and A. A. Soluyanov, Nature (London) **538**, 75 (2016).
[16] Z. Yan and Z. Wang, Phys. Rev. Lett. **117**, 087402 (2016).
[17] G. E. Volovik, Phys. Scr. **T164**, 014014 (2015).
[18] Q. Xu, R. Yu, Z. Fang, X. Dai, and H. Weng, Phys. Rev. B **95**, 045136 (2017).
[19] C. Fang, H. Weng, X. Dai, and Z. Fang, Chin. Phys. B **25**, 117106 (2016).
[20] Y. Kim, B. J. Wieder, C. L. Kane, and A. M. Rappe, Phys. Rev. Lett. **115**, 036806 (2015).
[21] T. Hyart, R. Ojajärvi, and T. T. Heikkilä, J. Low Temp. Phys. **191**, 35 (2018).
[22] H. Weng, Y. Liang, Q. Xu, R. Yu, Z. Fang, X. Dai, and Y. Kawazoe, Phys. Rev. B **92**, 045108 (2015).
[23] J. T. Wang, H. Weng, and C. F. Chen, Adv. Phys. X **4**, 1625724 (2019).
[24] Y. Cheng, J. Du, R. Melnik, Y. Kawazoe, and B. Wen, Carbon **98**, 468 (2016).
[25] J. T. Wang, H. Weng, S. Nie, Z. Fang, Y. Kawazoe, and C. F. Chen, Phys. Rev. Lett. **116**, 195501 (2016).
[26] Y. Cheng, X. Feng, X. T. Cao, B. Wen, Q. Wang, Y. Kawazoe, and P. Jena, Small **13**, 1602894 (2017).
[27] Y. Chen, Y. Xie, S. A. Yang, H. Pan, F. Zhang, M. L. Cohen, and S. B. Zhang, Nano Lett. **15**, 6974 (2015).
[28] J. T. Wang, C. F. Chen, and Y. Kawazoe, Phys. Rev. B **97**, 245147 (2018).
[29] Z. Z. Li, J. Chen, S. Nie, L. F. Xu, H. Mizuseki, H. Weng, and J. T. Wang, Carbon **133**, 39 (2018).
[30] Z. Zhao, Y. Hang, Z. Zhang, and W. Guo, Phys. Rev. B **100**, 115420 (2019).
[31] Z. Zhao, Z. Zhang, and W. Guo, J. Mater. Chem. C **8**, 1548 (2020).
[32] X. Dong, M. Hu, J. L. He, Y. J. Tian, and H. T. Wang, Sci. Rep. **5**, 10713 (2015).
[33] X. Feng, Q. S. Wu, Y. Cheng, B. Wen, Q. Wang, Y. Kawazoe, and P. Jena, Carbon **127**, 527 (2018).
[34] J. T. Wang, Y. Qian, H. Weng, E. G. Wang, and C. F. Chen, J. Phys. Chem. Lett. **10**, 2515 (2019).
[35] J. T. Wang, S. Nie, H. Weng, Y. Kawazoe, and C. F. Chen, Phys. Rev. Lett. **120**, 026402 (2018).
[36] B. Bradlyn, L. Elcoro, J. Cano, M. G. Vergniory, Z. Wang, C. Felser, I. M. Aroyo, and B. Andrei Bernevig, Nature (London) **547**, 298 (2017).
[37] H. C. Po, A. Vishwanath, and H. Watanabe, Nat. Commun. **8**, 50 (2017).
[38] Z. Song, T. Zhang, Z. Fang, and C. Fang, Nat. Commun. **9**, 3530 (2019).
[39] Z. Song, T. Zhang, and C. Fang, Phys. Rev. X **8**, 031069 (2018).
[40] Z. Z. Li, J. T. Wang, H. Mizuseki, and C. F. Chen, Phys. Rev. B **98**, 094107 (2018).
[41] M. T. Yin, Phys. Rev. B **30**, 1773 (1984).
[42] R. L. Johnston and R. Hoffmann, J. Am. Chem. Soc **111**, 810 (1989).
[43] M. D. Knudson, M. P. Desjarlais, and D. H. Dolan, Science **322**, 1822 (2008).

[44] H. Vora and T. J. Moravec, J. Appl. Phys. **52**, 6151 (1981).

[45] R. K. Choudhary, S. C. Mishra, P. Mishra, P. K. Limaye, and P. U. Sastry, Trans. IMF **95**, 197 (2017).

[46] G. Kresse and J. Furthmüller, Phys. Rev. B **54**, 11169 (1996).

[47] R. Armiento and A. E. Mattsson, Phys. Rev. B **72**, 085108 (2005).

[48] P. E. Blöchl, Phys. Rev. B **50**, 17953 (1994).

[49] J. Heyd, G. E. Scuseria, and M. Ernzerhof, J. Chem. Phys. **118**, 8207 (2003).

[50] A. A. Mostofi, J. R. Yates, Y. S. Lee, I. Souza, D. Vanderbilt, and N. Marzari, Comput. Phys. Commun. **178**, 685 (2008).

[51] N. Marzari, A. A. Mostofi, J. R. Yates, I. Souza, and D. Vanderbilt, Rev. Mod. Phys. **84**, 1419 (2012).

[52] Q. S. Wu, S. N. Zhang, H. F. Song, M. Troyer, and A. A. Soluyanov, Comput. Phys. Commun. **224**, 405 (2018).

[53] A. Togo, F. Oba, and I. Tanaka, Phys. Rev. B **78**, 134106 (2008).

[54] F. D. Murnaghan, Proc. Natl. Acad. Sci. USA **30**, 244 (1944).

[55] F. Occelli, P. Loubeyre, and R. LeToullec, Nat. Mater. **2**, 151 (2002).

[56] M. Z. Hasan and C. L. Kane, Rev. Mod. Phys. **82**, 3045 (2010).

[57] X. L. Qi and S. C. Zhang, Rev. Mod. Phys. **83**, 1057 (2011).

[58] G. Bian, T. R. Chang, R. Sankar, S.-Y. Xu, H. Zheng, T. Neupert, C.-K. Chiu, S.-M. Huang, G. Chang, I. Belopolski, D. S. Sanchez, M. Neupane, N. Alidoust, C. Liu, B. Wang, H.-T. Jeng, A. Bansil, F. Chou, H. Lin, and M. Z. Hasan, Nat. Commun. **7**, 10556 (2016).

[59] See Supplemental Material at http://link.aps.org/supplemental/10.1103/PhysRevB.101.205104 for (1) the two-band $k \cdot p$ model for oP16 and related carbon phases; (2) the lattice anisotropic effect on the shape of nodal lines; and (3) the strain-induced electronic band structures for oP16 carbon.